

Faceted Titania Nanocrystals Doped with Indium Oxide Nanoclusters As a Superior Candidate for Sacrificial Hydrogen Evolution without Any Noble-Metal Cocatalyst under Solar Irradiation

Vipin Amoli,[†] Malayil Gopalan Sibi,[†] Biplab Banerjee,[‡] Mohit Anand,[†] Abhayankar Maurya,[†] Saleem Akhtar Farooqui,[†] Asim Bhaumik,[‡] and Anil Kumar Sinha^{*,†}

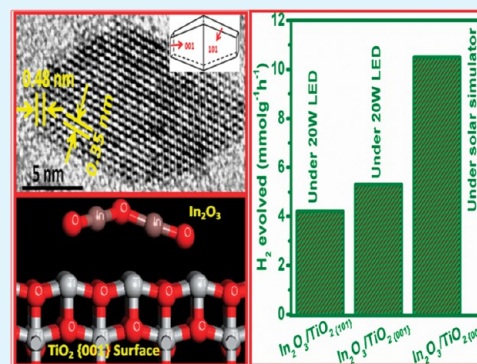
[†]CSIR–Indian Institute of Petroleum, Dehradun 248005, India

[‡]Department of Material Science, Indian Association for the Cultivation of Science, Jadavpur, Kolkata 700032, India

Supporting Information

ABSTRACT: Development of unique nanoheterostructures consisting of indium oxide nanoclusters like species doped on the TiO₂ nanocrystals surfaces with {101} and {001} exposed facets, resulted in unprecedented sacrificial hydrogen production (5.3 mmol h⁻¹ g⁻¹) from water using methanol as a sacrificial agent, under visible light LED source and AM 1.5G solar simulator (10.3 mmol h⁻¹ g⁻¹), which is the highest H₂ production rate ever reported for titania based photocatalysts, without using any noble metal cocatalyst. X-ray photoelectron spectroscopy (XPS) analysis of the nanostructures reveals the presence of Ti–O–In and In–O–In like species on the surface of nanostructures. Electron energy-loss spectroscopy (EELS) elemental mapping and EDX spectroscopy techniques combined with transmission electron microscope evidenced the existence of nanoheterostructures. XPS, EELS, EDX, and HAADF-STEM tools collectively suggest the presence of indium oxide nanoclusters like species on the surface of TiO₂ nanostructures. These indium oxide nanocluster doped TiO₂ (In₂O₃/Ti_{001}) single crystals with {101} and {001} exposed facets exhibited 1.3 times higher visible light photocatalytic H₂ production than indium oxide nanocluster doped TiO₂ nanocrystals with only {101} facets (In₂O₃/Ti_{101}) exposed. The remarkable photocatalytic activity of the obtained nanoheterostructures is attributed to the combined synergetic effect of indium oxide nanoclusters interacting with the titania surface, enhanced visible light response, high crystallinity, and unique structural features.

KEYWORDS: nanoheterostructures, indium oxide nanoclusters, faceted titania nanocrystals, sacrificial hydrogen production, synergetic effect, water splitting



INTRODUCTION

Solar energy driven water splitting to produce hydrogen, a clean renewable resource with zero emission, is an ultimate solution to the rapidly increasingly energy crisis and environmental pollution because of the dwindling resources of fossil fuels and harmful effects of greenhouse gases produced by combustion of the fuels.^{1–3} Since the pioneering work of Fujishima and Honda⁴ in 1972, a large number of photocatalytic materials such as oxides, nitrides, and sulfides have been synthesized and studied for water splitting.² Among these materials, TiO₂ has been intensively investigated over the past two decades due to its unique properties such as strong oxidative ability, high chemical stability, nontoxicity, low cost, as well as a wide range of industrial applications.^{5–7} Various kind of porous TiO₂ nanostructures with different morphology have widely been used for solar energy driven devices like dye-sensitized solar cells^{8,9} and photocatalytic water splitting.^{10,11} However, because of the intrinsic wide band gap of anatase TiO₂ (3.2 eV), only 5% of the solar energy incident on the earth surface can be utilized. In recent years, many attempts have been made to dope TiO₂ with transition metal ions such as Fe,¹¹ Au,¹² and Cu¹³ and

nonmetal elements such as C,¹⁴ N,¹⁵ and P,¹⁶ to extend the photoresponse of TiO₂-based systems further into the visible-light region. Nevertheless, hydrogen production efficiency from pure TiO₂ through the visible light driven photocatalytic water splitting reaction has proven to be extremely due to high recombination rate of photogenerated electrons and holes and large over potential for the generation of H₂ on the titania surface.^{17,18} To date, the deposition of noble metal nanoparticles such as Pt, Pd, and Rh (acting as cocatalyst) on the surface of TiO₂ has been massively investigated to inhibit the recombination between photogenerated electrons and holes to develop more efficient photocatalytic systems.^{1,5,6} Due to their perceived rarity, more research has been carried out to replace these noble metal cocatalysts without compromising with the efficiency of the device. Some reports suggest that the presence of other oxides species on the external surface of the TiO₂ framework can lead to the better visible light photo-

Received: October 21, 2014

Accepted: December 9, 2014

Published: December 9, 2014

activity of the composite.^{18,19,17} In recent years indium doped TiO₂ structures or In₂O₃/TiO₂ heterostructures have drawn considerable attention due to the wide range of their practical applications. Wang et al. reported the presence of unique surface chemical species on the surface of In-doped TiO₂ structures and evaluated their photocatalytic activity for photo degradation of 4-chlorophenol under visible light irradiation.²⁰ Armand et al. reported that indium doped TiO₂ materials have different surface properties than bulk, that might be used for engineering new devices with improved properties.²¹ Mu et al. reported that TiO₂-In₂O₃ heterostructures showed superior visible light photocatalytic activity to degrade rhodamine B.²² In₂O₃ is a relatively narrow bandgap ($E_g = 2.8$ eV) semiconductor, in which both the conduction band (CB) and the valence bands (VB) lie above those of TiO₂ ($E_g = 3.0$ eV for rutile, $E_g = 3.2$ eV for anatase). Thus, when TiO₂ is coupled with In₂O₃, photogenerated electron transfer from CB of In₂O₃ to the CB of TiO₂ gives rise to an efficient separation of photogenerated excitons and responsible for superior performance of these heterostructures.²² Despite all of these merits, indium oxide-TiO₂ composites have not been considerably researched. Most of the composites which have been developed have been used only for photocatalytic degradation of organic molecules.²⁰⁻²² These benefits indicate that applications of In₂O₃/TiO₂ composites are likely to increase in the future.

Recently crystal facet engineering of semiconductor oxides has grown as an important area of scientific research and development.²³⁻²⁵ The unique properties of faceted crystals can be tuned with the help of morphology control, for applications such as photocatalysis,²⁶ water splitting,^{27,25} and energy devices.²⁸ Liu et al. demonstrated that nanosized anatase TiO₂ single crystals exhibited eight times higher photocatalytic activity than microsized anatase TiO₂ single crystals for water splitting to produce hydrogen.²⁹ Several reports claimed that efficient charge separation can be achieved through reactive selectivity of photogenerated charge carriers on {101} and {001} crystallographic facets in anatase TiO₂, which is highly desirable in solar energy driven phenomena.^{30,31} These reported findings indicated that development of narrow band gap semiconductor/TiO₂ heterostructure nanocomposites with {101} and {001} exposed facets can be a key to constructing semiconductor based devices for hydrogen production, solar cells, and photocatalysis. This inspires us to make indium oxide nanoclusters doped TiO₂ single crystals with {101} and {001} exposed facets, with superior properties like high crystallinity and better visible light response. We believe that these unique properties can lead to high photocatalytic activity of these materials, hence promoting their potential applications in solar energy driven processes to produce clean energy. Earlier reports²¹⁻²³ have not preferentially used (001) surfaces to stabilize indium oxide clusters, so the photoactivities reported earlier have not been as exceptionally high as observed by us.

Herein, we report novel nanoheterostructures consisting of indium oxide nanocluster like species doped on the TiO₂ nanocrystals with {101} and {001} exposed facets, prepared by a simple hydrothermal process. The process to produce faceted nanostructures is facile, easily scalable, and environmentally friendly, as compared to those reported in the literature. These novel nanoheterostructures were found to exhibit remarkable photocatalytic activity in terms of hydrogen evolution (10.3 mmol g⁻¹ h⁻¹) from water using methanol as a sacrificial agent under visible-light without using any noble metal cocatalyst. As elucidated by the results, the combined

effect of various factors such as formation of nanoheterostructures, presence of high energy TiO₂ {001} facets, high crystallinity, and enhanced visible light response of this unique material resulted in unprecedented visible-light photocatalytic performance.

EXPERIMENTAL SECTION

Materials and Reagents. Titanium(IV) isopropoxide (Ti{OCH(CH₃)₂}₄, 95% Alfa Aesar), indium(III) chloride (InCl₃, anhydrous 99.99% Alfa Aesar), ethanol (Merck, anhydrous), and nitric acid (70% Merck) were used as received during synthesis. Commercially available P25 TiO₂ nanoparticles (Sigma) and indium oxide nanoparticles (SRL) were used for comparison.

Synthesis of Indium Oxide Nanoclusters Doped TiO₂ (In₂O₃/TiO₂) Nanostructures. In a typical optimized experimental procedure, 0.5 g of InCl₃ was added to 5 mL of ethanol and stirred for 10 min at ambient conditions. To this 12.5 mL of titanium isopropoxide was added dropwise under continuous stirring. After that 50 mL of 0.1 M HNO₃ was added to the reaction mixture. Then the temperature was raised to 80 °C and the suspension was heated for 2 h with continuous stirring in a closed vessel, and after that the mixture was transferred to an autoclave and kept in a furnace at 150 °C for 24 h for crystallization under hydrothermal condition. After the hydrothermal treatment, the autoclave was allowed to cool to room temperature, and the product was collected by vacuum filtration, washed several times with distilled water, and finally dried at 80 °C for 12 h. In₂O₃/TiO₂{101} and In₂O₃/TiO₂{001} nanostructures were obtained as a result of calcination of dried power at 450 °C (10 °C min⁻¹) and 550 °C (10 °C min⁻¹) for 2.5 h, respectively. In₂O₃/TiO₂{101} refers to the sample with exposed {101} planes and In₂O₃/TiO₂{001} refers to samples with some exposed {001} planes (in addition to predominant {101} plane).

Photocatalytic Activity. The photocatalytic H₂ production experiments were performed in a photocatalytic reactor, which consisted of a 100 mL Pyrex round-bottom flask, the opening of which was sealed with silicon rubber septum at ambient temperature and atmospheric pressure and a high power 20W LED flood light (HP-FL-20W) lamp. It produced white light with a beam angle of 120 degree. The dimension of the lamp is 180 × 140 × 110 mm, operating at 86-265VAC and AC/DC12 V, manufactured by Hope LED Opto-Electric Co., Ltd. (Shenzhen), china. The material was also tested under an AM 1.5G solar simulator (Newport 94023A Oriol Sol3A, class AAA, power output: 100 mW/cm², lamp power: 450W) as light source (emission spectrum is given in the Supporting Information (SI), Figure S1). In a typical run, flask containing 0.1 g of each sample suspended in 20 mL of a solution of water/methanol (vol 1:1) under continuous stirring was positioned below the source and illuminated from the top of the flask. The ambient temperature of the flask was maintained at 25 °C. The evolved gases were collected after 1.5 h using an airtight gas syringe (Hamilton) and hydrogen content was immediately analyzed by gas analyzer (Aligent 7890) equipped with a thermal conductivity detector. The amount of oxygen generated during the photocatalysis of H₂O/CH₃OH mixture over different photocatalysts in our experimental conditions was calculated by GC after subtracting the amount of oxygen from air (20.9%) during sampling and analysis (corresponding to the detected nitrogen peak area) from total O₂ detected in GC.

In situ reaction monitoring using mid Infrared spectroscopy was performed for the activation of Methanol/Water (1:1) system with 1% In in TiO₂ catalyst in the presence of 20W LED Flood Light. A mid-IR Fiber-optic system "SYS-IRX Reaction View -X" from Remspec Corporation, USA was used and the data obtained was analyzed using "GRAMS/AI & GRAMS 3D (version 9.1)" part of "GRAMS Spectroscopy software suite" from Thermo Fisher Scientific Inc. Similar experimental set up as used for photocatalytic experiment was used. A background for the methanol/water system was taken and subtracted from all the spectra taken. Spectra were gathered continuously for 5.5 h with 37 scans in 1 min at 4 cm⁻¹ resolution.

Calculation Method. We used Forcite module provided by Accelrys Materials Studio 7.0. This module is an advanced classical

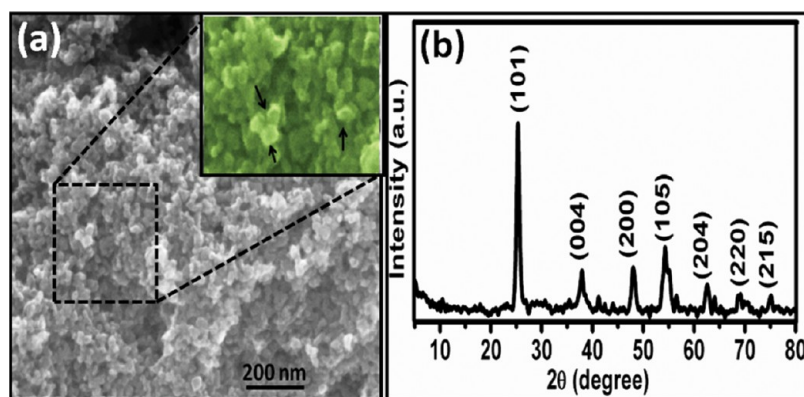


Figure 1. (a) FESEM image and (b) XRD pattern of $\text{In}_2\text{O}_3/\text{TiO}_2$ nanocrystals calcined at $550\text{ }^\circ\text{C}$ ($\text{In}_2\text{O}_3/\text{TiO}_{2(001)}$).

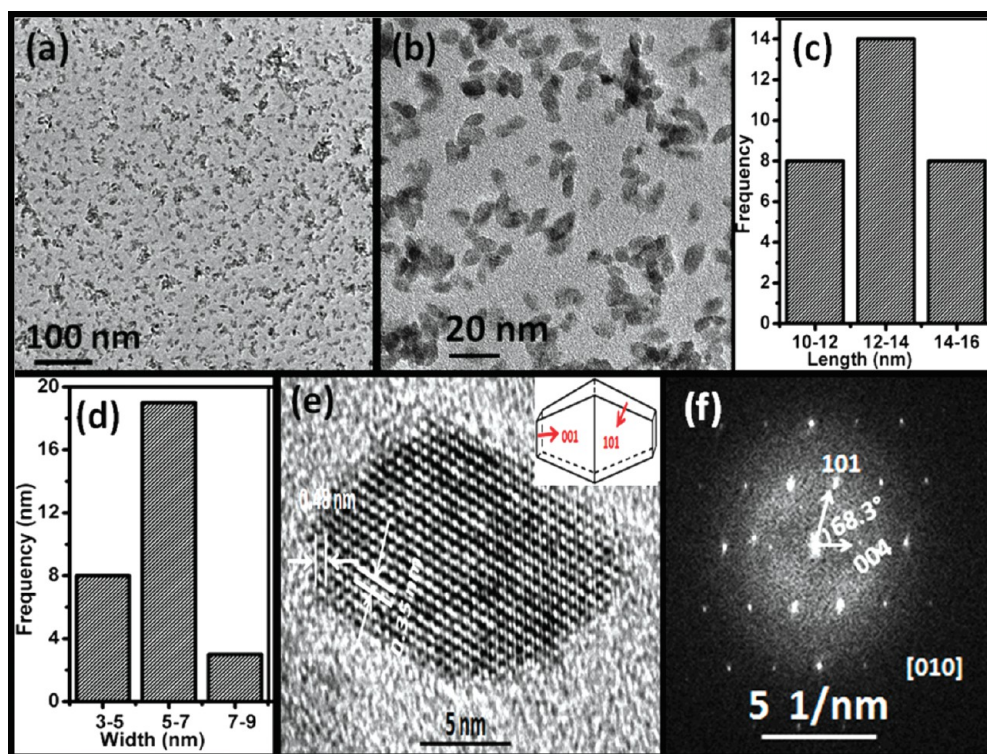


Figure 2. (a) TEM image of $\text{In}_2\text{O}_3/\text{TiO}_2$ nanocrystals prepared by calcination at $550\text{ }^\circ\text{C}$ ($\text{In}_2\text{O}_3/\text{TiO}_{2(001)}$), (b) TEM image of the same sample at a higher magnification, (c) length, (d) width distribution histograms of the nanostructures obtained from the panel b, (e) high-resolution TEM image showing individual nanocrystallite, Inset shows a model of truncated tetragonal bipyramid shape as exhibited by the sample, (f) the corresponding fast-Fourier transform (FFT) pattern.

mechanics tool that enables energy calculations, geometry optimizations, and dynamics simulations. Anatase TiO_2 surfaces (TiO_2 (101) and TiO_2 (001)) were built by taking lattice parameters for anatase are $a = 3.830\text{ \AA}$ and $c = 9.613\text{ \AA}$. Then the periodicity of the structures was changed by constructing a super cell, and then vacuum slab of thickness 20 \AA on the top of the (101) and (001) surface of the super cell was used to eliminate the interaction between the neighbor cells. To get accurate results, we first optimized the crystal structures and atomic coordinates, by minimizing the energy and atomic forces. The indium oxide cluster (In_2O_3) was stabilized using Dmol3 code in the Materials Studio 7.0 package using generalized gradient approximation (GGA) with Perdew–Burke–Ernzerhof (PBE) correlation. The linear stick structure chosen (Figure S2 in SI) before optimization refines to a “flying gull” having O–In–O bond angle of 131.78° shown in and agrees well with the previous report.³² Then we studied the $\text{In}_2\text{O}_3/\text{TiO}_{2(101)}$ and $\text{In}_2\text{O}_3/\text{TiO}_{2(001)}$ systems using universal force field in Forcite module tool to calculate energy calculations, geometry

optimizations, when indium oxide cluster (In_2O_3) was present on the TiO_2 (001) and TiO_2 (101) surfaces. In all the calculations, the bottom TiO_2 layers were fixed, only the atoms in the upper two layers in the super cell and indium oxide cluster (In_2O_3) (previously stabilized) were free to relax. The convergence tolerance was set as 0.001 kcal/mol for energy and 0.5 kcal/mol \AA for force in 1000 iterations in the geometry optimization process.

Characterization. X-ray diffraction (XRD) patterns of the samples were recorded on Bruker D8 Advance Diffractometer operating in the reflection mode with $\text{Cu K}\alpha$ radiation (40 kV , 40 mA). Surface morphology of the samples was obtained using field emission scanning electron microscopy (FESEM, Quanta 200F, Netherlands). Field emission gun transmission electron microscope JEOL-TEM-2010, operating at 200 kV was used for high-resolution transmission electron microscope (HRTEM) images. High angle annular dark field-scanning transmission electron microscopic (HAADF-STEM) images were obtained by an ultrahigh resolution field emission gun coupled with a

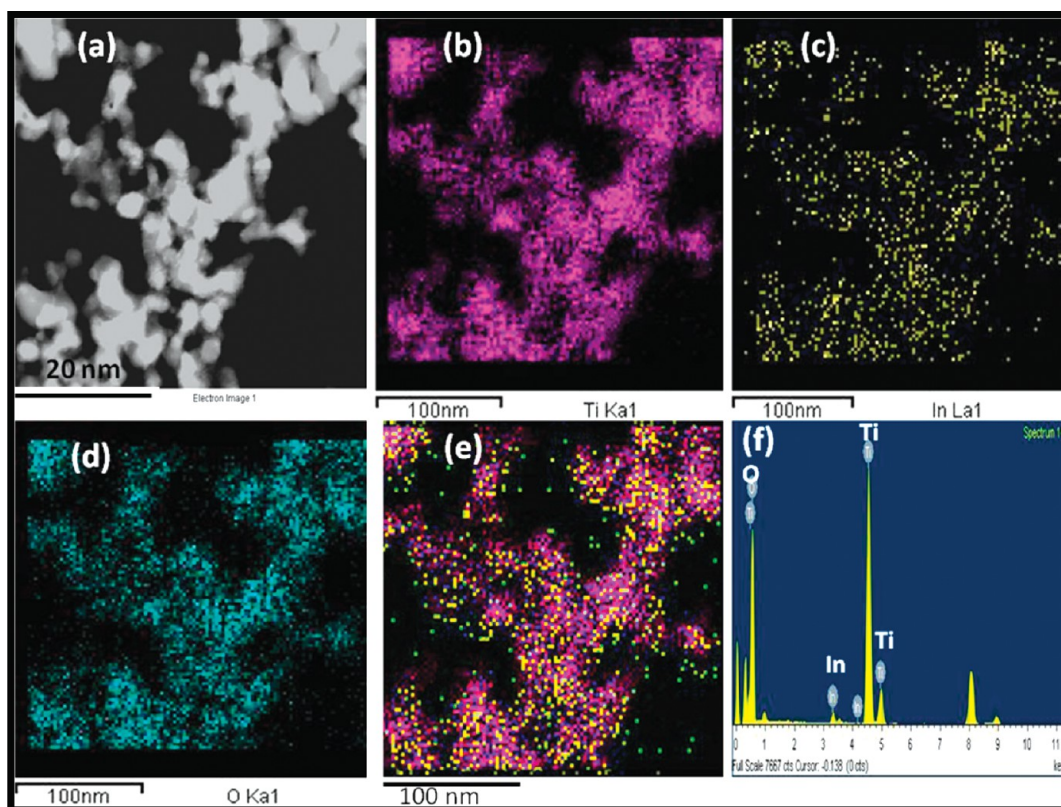


Figure 3. (a) HAADF-STEM image of the sample: Elemental maps obtained by X-EDS for (b) Ti, (c) In, (d) O, (e) In and Ti together, and (f) EDX of the sample.

HAADF detector and an energy-dispersive X-ray (EDX) spectrometer equipped in this transmission electron microscope. X-ray photoelectron spectroscopy was performed on Axis-Ultra DLD, Shimadzu Instrument equipped with an Mg K α X-ray exciting source with 30 mA current, 15 kV voltage, and 80 eV pass energy. The energy scale was calibrated using Au. The UV–vis spectra of the samples were recorded on a PerkinElmer model Lambda 19 for wavelength ranges from 200 to 800 nm. The Brunauer–Emmett–Teller (BET) specific surface area, Barrett–Joyner–Halenda (BJH) calculated average pore size, and pore volume of the samples were obtained from the N₂ adsorption/desorption isotherms recorded on BELSORP max (Japan) at 77 K. The samples were degassed and dried under a vacuum system at 150 °C for 2–3 h prior to the measurement. Raman spectra of the samples were recorded in a Triple Raman spectrometer (model-T64000; J-Y Horiba) equipped with 1800 grooves/mm gratings, TE Cooled Synapse CCD (J-Y Horiba) and with an open stage Olympus microscope with 50 \times objective. The samples were excited with a 514.5 nm wavelength laser from a Ar⁺ laser (model: Stabilite 2017, Spectra Physics). The integration time, number of accumulation (averaging), and laser power used for the analysis was 20 s, 4 times, and 500 micro Watt, respectively.

RESULTS AND DISCUSSION

The morphology of the In₂O₃/TiO₂ nanoparticles calcined at 550 °C (In₂O₃/TiO₂₍₀₀₁₎) was first examined by electron microscopy. Figure 1a (FE-SEM) revealed that product was composed of nanocrystals of sizes ranging from 15 to 30 nm. Inset is a high magnification image of the area represented by white rectangle. Nanocrystals showing truncated bipyramidal shape are indicated by black arrows, even though some irregular particles as a consequence of particle attachment can also be observed. Figure 1b shows a typical XRD pattern of the product in which all the diffraction peaks can be indexed to anatase TiO₂ (JCPDS no. 21-1272).²⁸ No separate peaks due to indium

oxide were observed, indicating that its crystallite size in the nanostructures is below the detection limit of XRD. The diffraction peaks for In₂O₃/TiO₂ nanostructures were almost similar (without any shift) in shape and position, as compared to pure TiO₂, prepared under identical experimental conditions (SI, Figure S3). The ionic radius of the guest In³⁺ ion (81 pm) is larger than that of the host lattice Ti⁴⁺ ion (53 pm);²⁰ therefore, both the interstitial and substitutional doping of In³⁺ in TiO₂ lattice can be discarded, which is supported by our XRD results. Hence it is considered that In³⁺ ions are located on the TiO₂ surface. The average crystallite sizes of the nanostructures were estimated from the (101) and (004) diffraction peaks using the Scherrer equation to be 14 and 5.3 nm, respectively.

Figure 2 shows the TEM images of In₂O₃/TiO₂ nanoparticles calcined at 550 °C (In₂O₃/TiO₂₍₀₀₁₎). Well separated and similar nanocrystals without noticeable aggregation can be observed in the low resolution TEM image (Figure 2a). Most of the particles have well-faceted rice grain like shapes (Figure 2b). Figure 2c,d showed length and width distribution histograms of the nanostructures with an average length of 13.3 nm and an average width of 5.8 nm. Comparing with the XRD results, the average length and width estimated using the TEM image (Figure 2b) correspond to average crystallite size obtained for (101) and (004) peaks, respectively. A random selection of 30 particles was used for size statistics of the sample. HR-TEM image (Figure 2c) revealed highly crystalline nature of the nanostructures with two sets of lattice fringes. The fringe spacing of 0.35 nm corresponds to the {101} planes while the fringe spacing of 0.48 nm corresponds to the {001} planes, indicating that flat surfaces should be {001} facets.³³ The drawing (lower right inset) shows a model of truncated

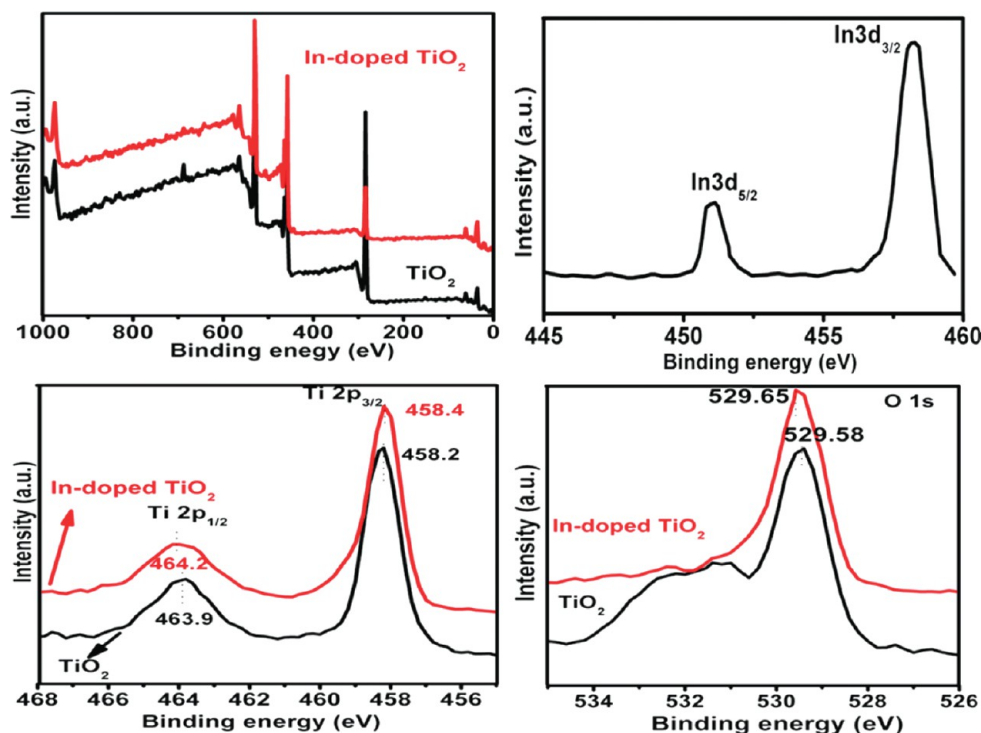


Figure 4. (a) XPS fully scanned spectra of the pure TiO_2 and $\text{In}_2\text{O}_3/\text{TiO}_2$ nanoheterostructures, (b) XPS spectrum of In 3d for the $\text{In}_2\text{O}_3/\text{TiO}_2$ nanoheterostructures, (c) XPS spectra of Ti 2p for $\text{In}_2\text{O}_3/\text{TiO}_2$ nanoheterostructures and pure TiO_2 , and (d) XPS spectra of O 1s for $\text{In}_2\text{O}_3/\text{TiO}_2$ nanoheterostructures and pure TiO_2 .

bipyramidal shape exhibited by as obtained In-doped TiO_2 nanocrystals with six $\{101\}$ and two $\{001\}$ facets as predicted. Shape of anatase is slightly truncated tetragonal bipyramidal enclosed by a majority of $\{101\}$ and a minority of $\{001\}$ by Wulff construction from surface energy considerations.³³ For this sample $\{001\}$ facets are obtained with a percentage of around 5.6, obtained from the degree of truncation.³³ The selected area electron diffraction (SAED) pattern can be indexed as the $[010]$ zone axis diffraction, and the diffraction spots can be assigned to (101) and (004) planes. The interfacial angle between $\{101\}$ and $\{001\}$ facets is measured to be 68.3° that agrees well with previous reports (Figure 2d).^{33,34} This sample with some exposed $\{001\}$ planes (in addition to predominant $\{101\}$ plane) was named as $\text{In}_2\text{O}_3/\text{TiO}_2\{001\}$.

A high-angle annular dark field scanning TEM (HAADF-STEM) image of the material having pronounced contrast difference within each nanostructure is demonstrated in Figure 3a. Under HAADF imaging conditions, the difference in the contrast can be directly correlated to a noticeable change in composition. X-EDS elemental mapping was performed to estimate the elemental distribution of Ti (Figure 3b), In (Figure 3c), and O (Figure 3d) elements present within the material. Elemental maps of Ti and In (Figure 3b,c) reveal their presence in the independent domains in the nanostructures such as outer and inner regions of the nanostructures coinciding with the dark and white contrast regions in HAADF image of Figure 3a. The overlay image Figure 3e reveals that indium species is not homogeneously dispersed over the TiO_2 nanostructures, which suggests a kind of heterostructure in which indium is dispersed site specifically on the surface of TiO_2 nanostructures in the form of indium oxide nanoclusters ($(\text{In}_2\text{O}_3)_n$), as also predicted in the literature.³² EDX spectrum (Figure 3f) indicates In, Ti, and O elements

existed in the sample. The calculated atomic percentages of Ti, In, and O are 32.87, 1.37, and 65.76 respectively, close to the nominal values.

In order to investigate the surface chemical states of all the elements, comparison between the XPS spectra from surface of pure and $\text{In}_2\text{O}_3/\text{TiO}_2$ nanostructures is shown in Figure 4. The presence of indium was not obvious from the survey spectrum as shown in Figure 4a but was clearly resolved in high-resolution spectra. The high-resolution peaks observed at binding energies of 451.1 and 458.1 eV corresponds to In 3d (Figure 4b), which can be assigned to In $3d_{5/2}$ and In $3d_{3/2}$, respectively.³⁵ This confirmed the presence of indium atoms on the TiO_2 surface. The high-resolution XPS spectra with scanning over the area corresponding to the binding energies for the Ti 2p region around 460 eV were analyzed in Figure 4c. The peak located at 464.2 eV corresponds to the Ti $2p_{1/2}$, and another one located at 458.4 eV was assigned to Ti $2p_{3/2}$, indicating the Ti^{4+} state^{36,22} in the indium doped TiO_2 sample. Figure 4d presented the O 1s photoelectron peaks. The peak located at 529.6 eV can be attributed to Ti–O–Ti (lattice O), and the shoulder located at 531.4 eV can be assigned to OH species on the surface.^{20–22}

After indium doping all the Ti 2p and O 1s peaks become slightly unsymmetrical, probably due to the formation of Ti–O–In species on the surface, but there is little shift in the Ti 2p and O 1s binding energies. In our sample Ti–O–In–Cl_x and O–Ti–Cl like species are not observed as reported by Wang et al.²⁰ It is believed that in our experimental conditions, InCl_3 gets completely hydrolyzed to form $\text{In}(\text{OH})_3$. Interestingly, the shoulder at 531.4 eV due to the hydroxyl species in pure TiO_2 is not observed in $\text{In}_2\text{O}_3/\text{TiO}_2$ nanostructures, which indicates the formation of In–O–Ti type linkages, which replace the OH[−] groups on the surface. On the basis of XRD, EDS, and

XPS results it can be concluded that indium is present in the form of well dispersed indium oxide on the surface of obtained nanostructures and is electronically interacting with the surface.

UV–visible absorption spectra of pure TiO₂ and In₂O₃/TiO₂ (In₂O₃/TiO₂{001} and In₂O₃/TiO₂{101}) composite nanostructures are shown in Figure 5. The absorption onset of pure TiO₂

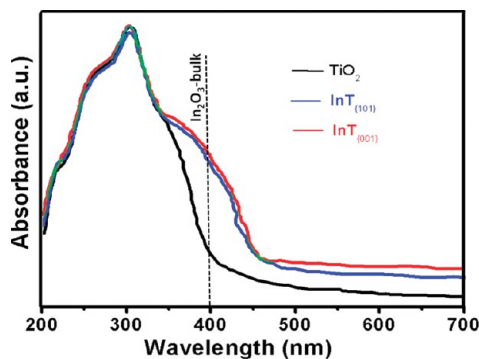


Figure 5. UV–vis absorption spectra of In₂O₃/TiO₂ nanoheterostructures and pure TiO₂.

was approximately at 390 nm, which agrees well with the bandgap of bulk anatase ($E_g = 3.2$ eV). Due to the relatively narrow band gap of In₂O₃ ($E_g = 2.8$ eV), In₂O₃/TiO₂ (In₂O₃/TiO₂{001} and In₂O₃/TiO₂{101}) composite nanostructures displayed red shifts in the absorption onset at 450 nm and an enhanced absorption in the visible-light region. This suggests formation of nanoheterostructures (detected by STEM, EELS elemental maps) and a band gap narrowing as a result of In³⁺ doping on the surface of TiO₂ nanostructures (evident by XPS) that agrees well with the literature.^{37,38,20} This suggests that In₂O₃/TiO₂{001} and In₂O₃/TiO₂{101} composite nanostructures can absorb solar energy over a broad range in the visible region, which is highly desirable for visible light photoactivity of photocatalyst.

FT-IR spectra (Figure S4 in the SI) of pure TiO₂ and In₂O₃/TiO₂ nanoheterostructures having different indium contents have several marked differences which is attributed to strong interactions and bondings between indium and titanium oxides. The Ti–O stretching frequency for the titania framework is clearly present near 500 cm⁻¹.³⁹ It is clearly observed that the mean position of the Ti–O linkage shifts from 500 cm⁻¹ in the pure TiO₂ to 539.7 and 540.6 cm⁻¹ in the In₂O₃/TiO₂ nanoheterostructures. Interestingly, in In₂O₃/TiO₂ nanoheterostructures the appearance of peaks at 461.4 and 472.6 cm⁻¹, with a noticeable shift toward higher wavenumber compared with the signature of In–O phonon vibration mode (429 cm⁻¹) in pure cubic In₂O₃, is observed.⁴⁰ Shifting of signature peaks for both Ti–O and In–O in In₂O₃/TiO₂ nanoheterostructures compared to their pure counterparts (TiO₂ and In₂O₃) indicates strong interactions between In₂O₃ nanocluster and TiO₂ in the In₂O₃/TiO₂ nanoheterostructures. These strong interactions between In₂O₃ nanoclusters and TiO₂ surfaces provides the effective synergy between In₂O₃ nanoclusters and TiO₂ surfaces that give rise to unique properties to In₂O₃/TiO₂ nanoheterostructures as described below.

Figure 6 compares Raman spectra of pure TiO₂ and In₂O₃/TiO₂ nanostructures with different indium contents. The specific vibration modes are located around 195 cm⁻¹ (B_{1g}), 395 cm⁻¹ (A_{1g}), 515 cm⁻¹ (B_{2g}), 637 cm⁻¹ (E_g), indicating the presence of the anatase phase in all of these samples.¹⁹ In case

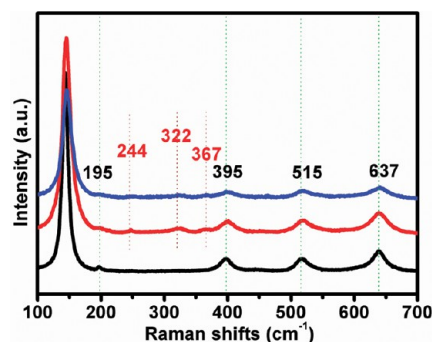


Figure 6. Raman spectra of (black) pure TiO₂, (blue) In₂O₃/TiO₂ nanoheterostructures (1 at % In content), and (red) In₂O₃/TiO₂ nanoheterostructures (2 at % In content).

of In₂O₃/TiO₂ nanostructures some additional weak peaks around 244, 322, and 367 cm⁻¹ were observed for the In₂O₃/TiO₂ samples. The bands at 244 and 367 cm⁻¹ are assigned to bending and stretching modes of O–In–O.^{41,37} The scattering peak at 322 cm⁻¹ in In₂O₃/TiO₂ nanoheterostructures is ascribed to bending vibration δ (InO₆) of octahedrons, which is shifted to higher wavenumber compared to a previous report.⁴¹

The higher wavenumber in our case may be due to the phonon confinement in indium oxide nanoclusters. Several reports claim that the phonon interactions are altered due to the effects of dimensional confinement on the phonon modes in nanoscale structured materials.⁴² It is noted that all the scattering peaks for In₂O₃/TiO₂ samples are shifted slightly toward higher wavenumber as compared to pure TiO₂, owing to the strong interaction of TiO₂ and In₂O₃ nanoclusters (present on the surface of TiO₂ nanostructures) in In₂O₃/TiO₂ nanostructures.

To gain a better understanding of formation of these In₂O₃/TiO₂ faceted nanocrystals, product is calcined at different temperatures and analyzed by XRD, FESEM, HRTEM, and N₂-sorption techniques. FESEM images (Figure S5, in the SI) of the product at 150 °C clearly showed highly agglomerated irregularly shaped particles with average size of ~10 nm. The particles were homogeneous, uniform, and dense. Figure 7 shows TEM images of the product. Network of nanoparticles aggregates can be seen in the low resolution TEM images (Figure 7a,b). Figure 7c showed particle size distribution in the range of 2–7 nm range with majority of particles in 4–5 nm in size. Randomly oriented nanocrystallites ranging in size from 4–6 nm with an interlaced structures were dominant products in the HRTEM image shown in Figure 7d. Weak diffraction spots in the SAED pattern (inset), indicating low crystallinity of the material. Figure 7e represents HRTEM image of an individual particle. The spacing between the adjacent layers was 0.35 nm, which corresponds to the distance between the (101) planes in the anatase structure. The XRD of the material at 150 °C shows some broad and low intensity peaks (Figure 7f). This is because the crystal domains are very small (3–5 nm). The crystal size estimated from the full width at half-maximum of the (101) peak using the Scherrer equation indicated that these TiO₂ nanocrystals were 5 nm in size which agrees well with TEM results.

Figure S6 of the SI shows the FESEM images of the sample after calcination at 450 °C. Low resolution TEM images (Figure 8a, b) show porous integrity of the nanostructures. Figure 8c shows particle size distribution in the range of 6–13 nm with majority of particles 8–9 nm in size. Figure 8d

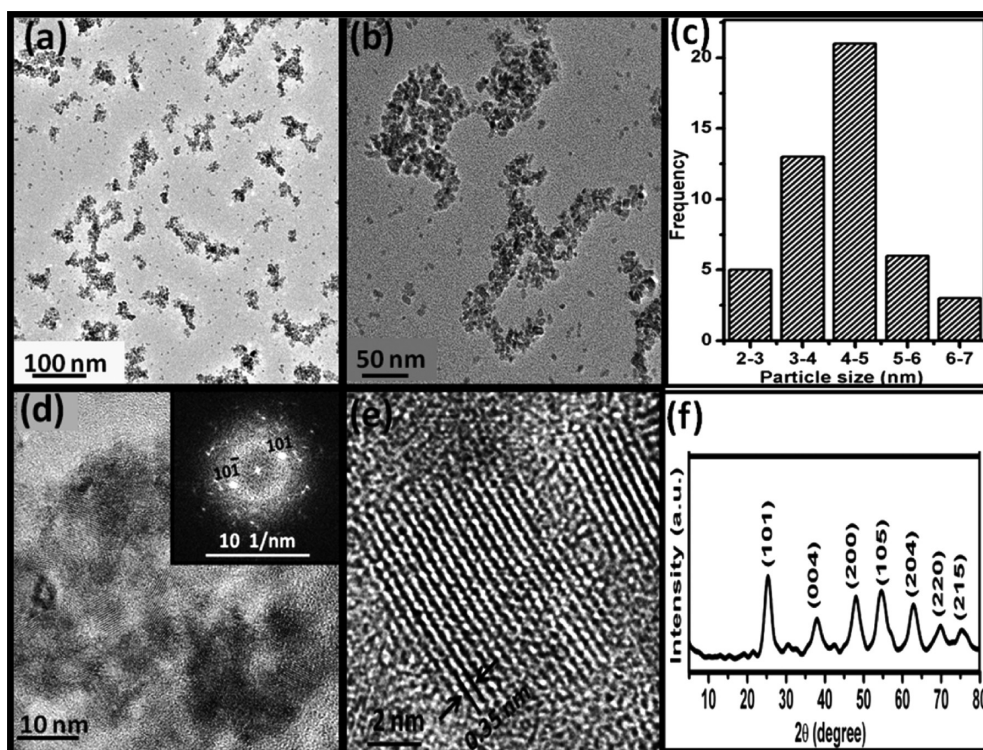


Figure 7. (a, b) TEM image of $\text{In}_2\text{O}_3/\text{TiO}_2$ nanocrystals prepared at 150°C , (c) histogram shows particle size distribution, (d) high magnification shows randomly oriented nanocrystallites with an interlaced structures, inset shows SAED pattern, (e) HRTEM image showing individual (101) anatase nanocrystallite, and (f) XRD pattern of the sample.

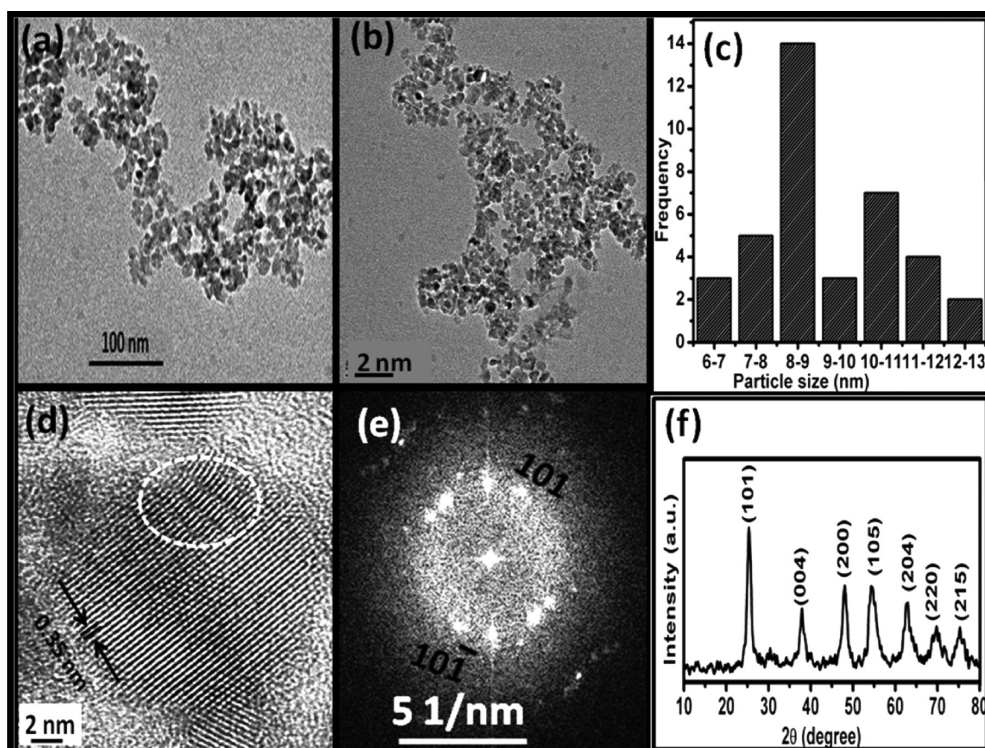


Figure 8. (a, b) TEM image of $\text{In}_2\text{O}_3/\text{TiO}_2$ nanocrystals calcined at 450°C ($\text{In}_2\text{O}_3/\text{TiO}_{2(101)}$), (c) histogram shows particle size distribution, (d) HRTEM image showing individual (101) anatase nanocrystallite, (e) SAED pattern, and (f) XRD pattern of the sample.

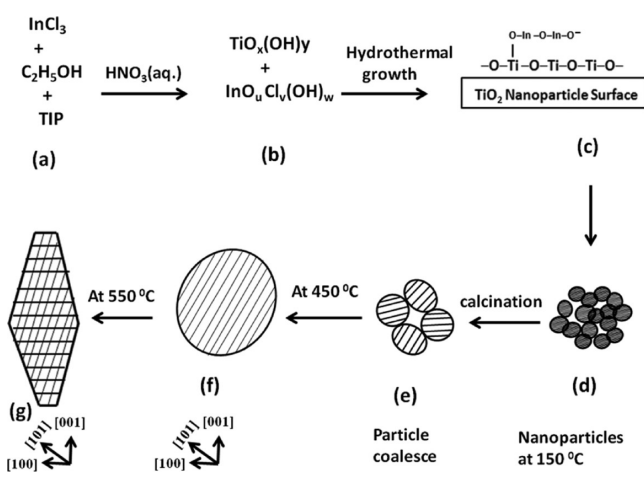
represents the HRTEM image of a single particle. Clear lattice fringes of separation 0.35 nm correspond to the (101) plane in anatase TiO_2 . The presence of few dislocations in the region (marked by white frame) may be due to the slight

misorientation of the nanoparticles during coalescing. Bright diffraction spots in the SAED pattern (Figure 8e), indicate high crystallinity of the material. Increase in the intensity of the 101 peak in the XRD (Figure 8f) pattern proves that crystallinity of

the sample improves with an increase in calcination temperature shown in. The particle size measured using the Scherrer equation to the 101 peak of the XRD was estimated to be 9 nm which agrees well with the TEM results. The increase in crystallinity is due to the thermally induced particles coalescence and grain growth.

On the basis of the above characterization results, we propose a mechanism for the formation of TiO_2 nanocrystals having indium oxide nanoclusters like species on the surface and change in exposed facets of these nanocrystals during calcination (Scheme 1). During the early stages of the synthesis

Scheme 1. Proposed Mechanism for the Development of $\text{In}_2\text{O}_3/\text{TiO}_2$ Nanoheretostructures by Formation of TiO_2 Nanocrystals Having Indium Oxide Nanoclusters Like Species on the Surfaces and Change in Exposed Facets during Calcination



process, titanium isopropoxide hydrolyzes with water and an aquo complex is initially formed which polymerizes to produce titanium oxo/hydroxo complex precipitates (Scheme 1b).⁴³ Reactivity of transition metal alkoxide precursors is very high compared to other metal alkoxides because of their incomplete d-subshell electronic configuration which helps to change the co-ordination ability and oxidation states.⁴⁴ At the same time, due to the delayed hydrolysis of indium precursor, indium oxo/hydroxo complex is not formed so effectively and during the growth process under the hydrothermal condition indium is dispersed in the form of indium oxide nanoclusters on the surface of titania nanocrystals (Scheme 1c). At 150 °C, formation of interconnected spherical nanoparticles of sizes $\sim 3\text{--}5$ nm takes place (Scheme 1d). At this early stage, surface area, mean pore diameter and the pore volume of the sample were $242\text{ m}^2/\text{g}$, 4.9 nm , and $0.29\text{ cm}^3/\text{g}$, respectively (Figure 9a). As the calcination temperature is increased, sorption curve of the sample exhibited relatively smaller hysteresis loop and the mean pore diameter peak shifts to larger value at elevated temperature. After calcination at 450 °C, surface area, mean pore diameter and the pore volume of the sample were $123\text{ m}^2/\text{g}$, 8.0 nm , and $0.25\text{ cm}^3/\text{g}$, respectively (Figure 9b).

Decrease in surface area and increase in mean pore diameter with increase in calcination temperature is due to the coarsening of nanoparticles and neck formation among the particles as seen in SEM images (SI, Figure S4). Crystallinity of the material increases and average crystallite size increases from 5 to 8 nm at 450 °C and 13 nm at 550 °C (Scheme 1e–g),

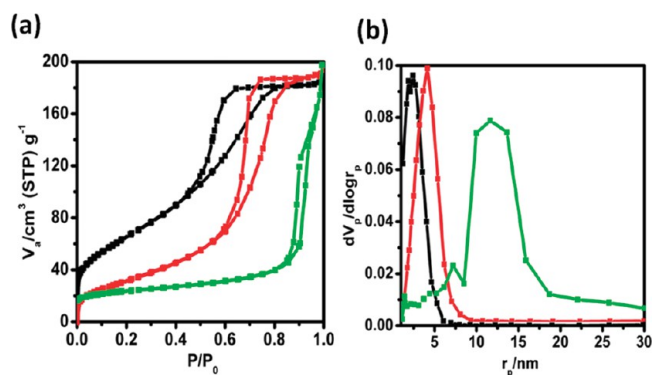


Figure 9. (a) Nitrogen adsorption–desorption isotherms of $\text{In}_2\text{O}_3/\text{TiO}_2$ nanocrystals: (black) at 150 °C, (red) calcined at 450 °C, and (green) calcined at 550 °C. (b) Pore size (BJH) distributions of indium oxide nanoclusters doped TiO_2 samples: (black) at 150 °C, (red) calcined at 450 °C, and (green) calcined at 550 °C.

indicative of particle coalescence and grain growth. After calcination at 550 °C, surface area, mean pore diameter, and the pore volume of the sample were $59\text{ m}^2/\text{g}$, 30 nm , and $0.45\text{ cm}^3/\text{g}$, respectively. It is noticed that the morphological and physiological properties of the sample calcined at 550 °C are somewhat unusual. HRTEM results showed that spherical shaped nanoparticles formed earlier at 450 °C transformed into tetragonal bipyramidal shaped particles at 550 °C and the adsorption isotherm visibly changes from type II (450 °C) to type I (550 °C) according to IUPAC classification, which supports HRTEM results of modification in the morphology of the sample at 550 °C. At a temperature of 550 °C, crystal facet surface energy plays an important role. Due to high surface energy of $\{001\}$ face (0.90 Jm^{-2}) than $\{101\}$ face (0.44 Jm^{-2}), spherical nanoparticles obtained at 450 °C grow along $[001]$ direction and transformed into rice grain like particles. The faceting is the most favorable mechanism for minimizing particle surface energy as also reported previously in the literature.⁴⁵ When the product is calcined at temperature 600 °C, the rutile (110) peak is also observed in the product as shown in XRD (Figure S7 in the SI), as anatase to rutile phase transformation is particle size dependent and energetically most favorable above an average critical size of $\sim 14\text{ nm}$ as claimed in many reports.⁴⁶

Figure 10 shows hydrogen production over $\text{In}_2\text{O}_3/\text{TiO}_2\{001\}$ and $\text{In}_2\text{O}_3/\text{TiO}_2\{101\}$ nanostructures from water/methanol

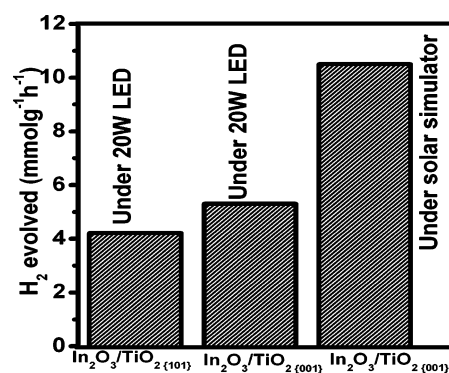


Figure 10. Photocatalytic hydrogen evolution of $\text{In}_2\text{O}_3/\text{TiO}_2$ nanostructures from water/methanol ($v/v = 1:1$) mixture under different irradiation light sources.

under different irradiation light sources. The H_2 production rate of $\text{In}_2\text{O}_3/\text{TiO}_2\{001\}$ nanoheterostructures ($5.3 \text{ mmol h}^{-1} \text{ g}^{-1}$) is higher (1.3 times) than that of $\text{In}_2\text{O}_3/\text{TiO}_2\{101\}$ ($4.2 \text{ mmol h}^{-1} \text{ g}^{-1}$) under visible light LED source. To ensure broader usefulness of our material and for comparison with the results reported in literature, photocatalysis was also carried out using solar simulator (with full solar spectrum, Figure S1, in the SI) for 1.5 h and a average value of $10.3 \text{ mmol h}^{-1} \text{ g}^{-1}$ is achieved, which is the highest reported hydrogen production rate ever reported for titania based photocatalyst without any noble metal cocatalyst, to date.^{47–49} and one of the highest H_2 production rates for any photocatalyst to date.^{50–53} Recently Zhao et al. reported the highest H_2 production rate ($37.6 \text{ mmol h}^{-1} \text{ g}^{-1}$) for carbon/ TiO_2 /carbon nanocomposites, using very expensive platinum as cocatalyst.⁴⁷ The cost obstacle of Pt used in this report may hinder its use for practical applications.

In our case, the process is facile and the H_2 production rate is remarkably high without any noble metal cocatalyst, which makes our material more attractive for practical applications. H_2 production profile (Figure S8 in the SI) shows that the H_2 production rate using the LED source is very high during the first 2 h, and thereafter the hydrogen production rate is slower. The saturation of the H_2 production rate is expected due to the steady–steady conditions, also reported by Narendranath et al. during photocatalytic H_2 evolution from the water–methanol system using $\text{InFeO}_3(\text{ZnO})_m$ oxides without any cocatalyst.⁵³ A controlled experiment with pure titania nanoparticles (P-25) under similar experimental conditions showed little hydrogen evolution ($0.2 \mu\text{mol h}^{-1} \text{ g}^{-1}$). Under similar experimental conditions pure indium oxide nanoparticles did not show any hydrogen production. Literature also predicts that both TiO_2 and In_2O_3 do not work individually as visible light photocatalyst toward water splitting.^{20–22} For the $\text{In}_2\text{O}_3/\text{TiO}_2$ sample with higher indium content (2 at. %) the H_2 production rate under similar experimental conditions is $1.74 \text{ mmol h}^{-1} \text{ g}^{-1}$ which is 3 times lower than that with lower indium content sample (1 at. %). This could be due to stronger interaction of the indium oxide cluster (at 1 at. %) with the titania support (specifically 001 planes) than that for larger indium oxide cluster (at 2 at. %). In our work, formation of nanoheterostructures ($\text{In}_2\text{O}_3/\text{TiO}_2\{001\}$, $\text{In}_2\text{O}_3/\text{TiO}_2\{101\}$) by combination of both oxides has resulted in excellent visible light photocatalyst for sacrificial H_2 production, which is clearly due to synergism between indium oxide nanoclusters (present on the surface TiO_2) and TiO_2 surfaces in our systems. This synergism between the indium oxide cluster and titania surface is also well supported by various characterization results discussed above.

Figure 11 compares the hydrogen evolution under steady-state conditions at different time intervals for $\text{In}_2\text{O}_3/\text{TiO}_2\{001\}$ and $\text{In}_2\text{O}_3/\text{TiO}_2\{101\}$ nanostructures. At each stage $\text{In}_2\text{O}_3/\text{TiO}_2\{001\}$ nanostructures are observed to be superior photocatalysts than $\text{In}_2\text{O}_3/\text{TiO}_2\{101\}$ nanostructures. Hydrogen production rate of $\text{In}_2\text{O}_3/\text{TiO}_2\{001\}$ nanostructures for different methanol–water v/v ratios under visible light (solar simulator) irradiation is represented in Figure 12.

It is clear from Table S2 (SI) that, as the methanol concentration increases, hydrogen production rate increases. For lower methanol–water v/v ratios (1:9–3:9) the hydrogen production rate is low, which increases sharply at (5:9) and then stays almost constant for higher methanol–water v/v ratios (7:9–9:9) with maximum hydrogen production rate at methanol–water v/v ratios 1:1. This proves that methanol not only acts as hole scavenger but also as electron enricher (more

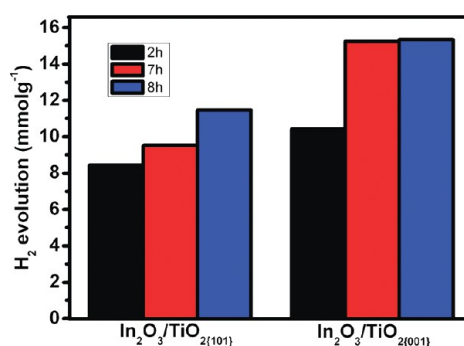


Figure 11. Photocatalytic hydrogen evolution of $\text{In}_2\text{O}_3/\text{TiO}_2$ nanostructures at different reaction time intervals: (black) 2 h, (red) 7 h, and (blue) 8 h under 20W LED source.

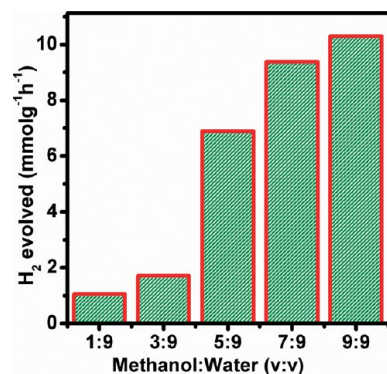


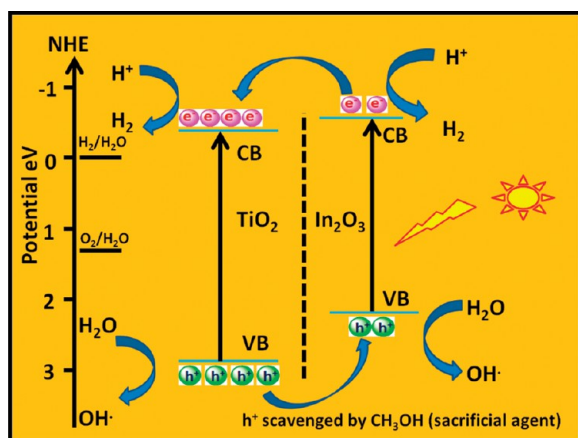
Figure 12. Photocatalytic hydrogen evolution of $\text{In}_2\text{O}_3/\text{TiO}_2\{001\}$ nanostructures with various methanol–water v/v ratios.

effectively at higher methanol–water v/v ratios) and contributes toward H_2 generation, as also reported previously.⁵³ On the basis of photocatalytic experimental results, the remarkable activity of the obtained photocatalyst can be attributed to the formation of a kind of nanostructures in which indium oxides nanoclusters like species are doped on the surface of TiO_2 nanocrystals and are preferentially stabilized on certain facets. These nanoclusters are found to tend toward dense, low symmetry structures approaching the bulk system at remarkably small molecular masses.³² In order to support our hypothesis, structures having indium oxide cluster stabilized on the TiO_2 (101) and (001) facets, before and after surface structure optimization are shown in Figure S9 a–d, (SI). In case of anatase TiO_2 (101) surface, it has a stepped structure with the $2cO$ along the [010] direction forming the edge of the step. After geometry optimization, a value of $-1162.07 \text{ kcal/mol}$ energy is obtained (SI, Figure S9b) for the system. In case of indium oxide cluster stabilized on anatase (001) surface, a value of $-3767.12 \text{ kcal/mol}$ energy is obtained after geometry optimization (Figure S8d, SI). Higher negative value of energy signifies the importance of {001} facets for indium oxide nanoclusters stabilization in $\text{In}_2\text{O}_3/\text{TiO}_2\{001\}$ nanostructures. Interestingly, it is observed that the initial shape of indium oxide cluster (flying gull) changed, during the process of geometry stabilization on {101} facet, while it remains unchanged on {001} facets to obtain the final structures for $\text{In}_2\text{O}_3/\text{TiO}_2$ systems. These experimental facts clearly suggested that indium oxide nanoclusters were more stabilized on {001} TiO_2 facets, that contributes to enhanced photoactivity of these $\text{In}_2\text{O}_3/\text{TiO}_2\{001\}$ nanostructures than $\text{In}_2\text{O}_3/\text{TiO}_2\{101\}$ nanostructures. Earlier reports^{19–21} have not looked into (001)

surfaces to stabilize indium oxide clusters, so the photoactivities reported earlier have not been as exceptionally high as observed by us.

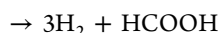
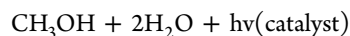
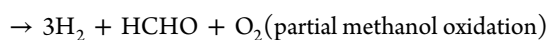
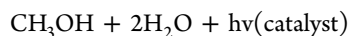
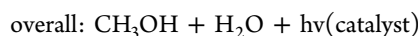
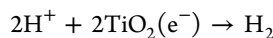
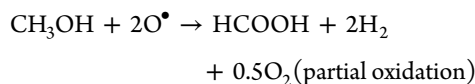
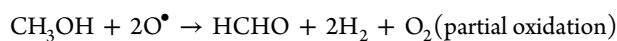
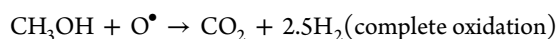
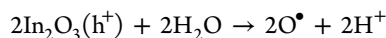
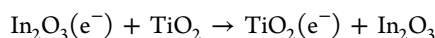
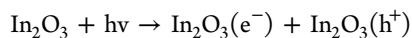
The charge transfer behaviors during the process are schematically illustrated in Scheme 2.

Scheme 2. Schematic Diagram Illustrating the Energy Band Positions and Photogenerated Electron-Hole Pair Separation in In₂O₃/TiO₂ Nanoheretostructures under Solar Light Driven Water Splitting Using Methanol As Hole Scavenger^a



^aCB = conduction band, VB = valence band, h⁺ = hole.

Under visible light irradiation, photogenerated electrons in In₂O₃ moved freely to the TiO₂, meanwhile, the photogenerated holes were left in the valence band of In₂O₃ with reacts with water molecule to generate [•]OH redical and H⁺ ion. The [•]OH radical, which is a strong oxidizing agent, decomposes methanol under different conditions. On the other hand H⁺ ions react with TiO₂ electrons (e⁻) to produce hydrogen. The mechanism for photocatalytic water splitting in our work is proposed as follows



Upon light irradiation, electrons from the valence bands (VBs) of In₂O₃ and TiO₂ are excited and subsequently promoted to their corresponding conduction bands (CBs), leaving behind holes as shown in Scheme 2. The conduction band of In₂O₃ lies (-0.63 V versus NHE) above the conduction band of TiO₂ (-0.4 eV versus NHE), as a result promoted electrons from the CB of In₂O₃ flow toward the CB of TiO₂ and photoinduced holes tend to migrate to the In₂O₃ because of more positive valence band of TiO₂.²² Thus, the effective charge separation is achieved in the nanostructures. This is a proof of the role of TiO₂ as host oxide for electron trapping generated during the e⁻ h⁺ pair generation as is illustrated in Figure 11. Also the accumulation of excess electrons in the CB of TiO₂ can cause upward shift in its Fermi level to assume a more negative redox potential compared to H⁺/H₂ (0 V Versus NHE).^{54,55} For efficient water splitting to produce H₂, the CB of the photocatalyst should be more negative than the reduction potential of H₂O to decrease in recombination of photo generated charges.^{56,57} It is a kind of sensitization of TiO₂ with In₂O₃ nanoclusters present on the surface of nanocrystals as evident by XPS, STEM, and EELS mapping. On the basis of characterization results, it is clear that the size of In₂O₃ nanoclusters (present on the surface of TiO₂) is very small. In this case quantum confinement effects might result in larger band gap for In₂O₃ nanoclusters than bulk In₂O₃. Previous reports claimed that quantum size effects are more pronounced in the conduction band than valence band for most of the semiconductors.^{58,59} The driving force for charge transfer between conduction bands in nanoscale heterojunctions is the conduction band offset, resulting from quantum confinement. This might be responsible for efficient charge transfer among the In₂O₃ nanoclusters and TiO₂ nanostructures in In₂O₃/TiO₂ nanoheretostructures, obtained by us. Importantly, In₂O₃/TiO₂{001} nanohereto-structures (with some {001} exposed along with {101} planes) show higher photocatalytic activity than In₂O₃/TiO₂{101} (with only {101} planes exposed) nanoheretostructures, despite similar UV-visible absorption spectra and lower surface area of the former. There are several reports which claim that not only the surface area but also the other factors such as crystallinity, surface atomic structure, crystallite size, photoexcited electron-hole lifetime and exposed crystals facets can play a key role in the photocatalytic activities of the materials.^{60,61} The better photocatalytic activity of In₂O₃/TiO₂{101} nanoheretostructures is attributed to many factors. First, crystallinity of In₂O₃/TiO₂{001} nanostructures is better than that of In₂O₃/TiO₂{101} nanostructures. In photocatalytic water splitting, photocatalyst having high crystallinity is advantageous to increase the probability of the reaction of photogenerated electrons and holes with water molecules by avoiding recombination.^{62,63} The calculated particle size for In₂O₃/TiO₂{001} nanostructures is 14 nm, which is critical to obtain high performance of the photocatalyst for water splitting to produce hydrogen. Second, in In₂O₃/TiO₂{001} nanostructures, 5.6% of the TiO₂ nanostructures surface being enclosed by high energy {001} facets as compared to In₂O₃/TiO₂{101} nanocrystals enclosed by pure {101} facets with no {001} facets, which is responsible to a great extent for the remarkable photoactivity of the former.

Many reports claim the difference of undercoordinated (such as penta-coordinated) Ti atoms present on {001} (with 100% penta-coordinated Ti) and {101} (with 50% penta-coordinated Ti and 50% hexa-coordinated Ti) surfaces.^{64,65} Each crystal facet owns its unique surface atomic arrangement resulting in different photocatalytic activity of the material,^{66,60} and crystal facet with a higher percentage of undercoordinated atoms is usually more reactive in the heterogeneous reactions.^{67–69} In case of $\text{In}_2\text{O}_3/\text{TiO}_2\{001\}$ nanocrystals, synergy between high energy {001} (oxidation site) and low energy {101} (reduction site) TiO_2 crystal facets, that allows the photogenerated e^-/h^+ pairs to be separated for a longer duration and makes such nanocomposite heretostructures more effective in the photocatalysis.^{64–66} Hence more efficient charge separation in the $\text{In}_2\text{O}_3/\text{TiO}_2\{001\}$ nanoheterostructures can be obtained via reduction reaction with photogenerated electrons and oxidation reaction with photogenerated holes, which takes place separately on the {001} and {101} facets under photo-irradiation. Third, simulation results show that In_2O_3 nanoclusters are more stabilized on {001} TiO_2 facets, consequently, efficient interfacial charge transfer to the adsorbed species leads to the better photocatalytic performance of $\text{In}_2\text{O}_3/\text{TiO}_2\{001\}$ nanostructures than $\text{In}_2\text{O}_3/\text{TiO}_2\{101\}$ nanoheterostructures.

In-situ reaction monitoring using mid Infrared spectroscopy results (Figure S10 in the SI) indicates multiple peaks in 1000–1300 cm^{-1} region, attributed to the presence of C–O stretching of ethers. Presence of strong bands at 1070–1170 cm^{-1} (SI, Figure S10a,b) indicates predominant presence of ethers. Small intensity two or more multiple bands of C=O stretching at 1700–1750 cm^{-1} (SI, Figure S10a,b) indicates formation of acids. Correspondingly acidic –OH stretch was also observed at 3275 cm^{-1} (SI, Figure S10c,e) and C=O stretch was observed between 1210–1320 cm^{-1} (SI, Figure S10a,b). Formation of aldehydes was confirmed by medium intensity bands of C=O stretching observed at 1744 cm^{-1} (SI, Figure S10a,b) and =C–H stretching at 2850 and 2730 cm^{-1} (SI, Figure S10e). Formation of alkanes in the reaction media was observed with C–H bending vibrations at 1450 cm^{-1} (SI, Figure S10a,b) and very strong C–H stretching observed at 2950 cm^{-1} (SI, Figure S10d). Variable stretching of C=C was also observed between 1500 and 1550 cm^{-1} (SI, Figure S10a,b). Formation of alkenes =C–H stretch (3040 cm^{-1}) and C=C variable stretching (1640–1660 cm^{-1}) and very strong =C–H bending (980 cm^{-1}) are also observed (SI, Figure S10a–c,e). Stretching of H-bonded –OH for alcohols was also observed at 3370 (SI, Figure S10c,e) and the stretching for CO_2 was very well observed at 2350 cm^{-1} (SI, Figure S10).

Absorbance of two intermediate compounds, –CHO (C=O 1744 cm^{-1}) and –COOH (C=O 1718 cm^{-1}), as a function of reaction time has been shown in Figure S11 in the SI, indicating the formation and disappearance of aldehyde and acidic intermediates. Further studies for predicting the reaction mechanisms and quantitative measurements of rate of formation and disappearance of the intermediate compounds are in progress. These would be necessary for better understanding of these reactions. Calculations based on rate of appearance/disappearance of H_2 and CO_2 , SI, Table S2, indicates that 91% of total H_2 produced is by photo catalytic water splitting and only 9% of the total H_2 produced is from photo catalytic decomposition of methanol to CO_2 . Quantification of other reactions taking place simultaneously needs to be studied in detail and will be provided in our next work.

CONCLUSIONS

A new kind of nanoheterostructure consisting of indium oxide nanoclusters like species doped on faceted TiO_2 nanocrystals have been obtained through a facile hydrothermal route. XRD, HRTEM, STEM, EELS, and XPS techniques establish indium oxide nanoclusters like species doped on the surface of TiO_2 nanostructures, preferentially on {001} facet, and formation of a kind of nanoheterostructures that are responsible for visible light activity of the material. The results demonstrate that the unique features of the material such as synergism between TiO_2 surface and In_2O_3 nanoclusters, enhanced visible light response, high crystallinity, high surface area, and presence of high energy {001} facets make it an excellent photocatalyst, which resulted in an unprecedented visible-light photocatalytic H_2 production rate of 10.3 $\text{mmol h}^{-1} \text{g}^{-1}$ under solar irradiation without using any cocatalyst. Our results open a new avenue to develop high-performance nanosized photocatalysts.

ASSOCIATED CONTENT

Supporting Information

Emission spectrum of solar simulator, optimized structure of indium oxide nanocluster, XRD patterns of pure TiO_2 and $\text{In}_2\text{O}_3/\text{TiO}_2$ nanocrystals, FT-IR spectra of pure TiO_2 and $\text{In}_2\text{O}_3/\text{TiO}_2$ nanoheterostructures, FESEM images of the sample prepared at 150 °C, FESEM images of the sample prepared at 450 °C, XRD patterns of $\text{In}_2\text{O}_3/\text{TiO}_2$ nanocrystals calcined at 600 °C, Product profiles for photocatalytic water/methanol splitting, optimized structures for $\text{In}_2\text{O}_3/\text{TiO}_2\{101\}$ and $\text{In}_2\text{O}_3/\text{TiO}_2\{001\}$ systems, in situ FTIR monitoring of photocatalytic experiment, and formation of intermediates during reaction. This material is available free of charge via the Internet at <http://pubs.acs.org>.

AUTHOR INFORMATION

Corresponding Author

*Tel.: 91-135-2525842. Fax: 91-135-266-203. E-mail: asinha@iip.res.in

Notes

The authors declare no competing financial interest.

ACKNOWLEDGMENTS

Director, IIP is acknowledged for approving the research; V.A. and M.G.S. kindly acknowledge CSIR and UGC, New Delhi for their fellowship.

REFERENCES

- (1) Ni, M.; Leung, M. K. H.; Leung, D. Y. C.; Sumathy, K. A Review and Recent Developments in Photocatalytic Water-Splitting using TiO_2 for Hydrogen Production. *Renew. Sust. Energy Rev.* **2007**, *11*, 401–425.
- (2) Maeda, K.; Domen, K. New Non-Oxide Photocatalysts Designed for Overall Water Splitting under Visible Light. *J. Phys. Chem. C* **2007**, *111*, 7851–7861.
- (3) Lu, D.; Takata, T.; Saito, N.; Inoue, Y.; Domen, K. Photocatalyst Releasing Hydrogen from Water. *Nature* **2006**, *440*, 295–295.
- (4) Fujishima, A.; Honda, K. Electrochemical Photolysis of Water at a Semiconductor Electrode. *Nature* **1972**, *238*, 37–38.
- (5) Kamat, P. V. TiO_2 Nanostructures: Recent Physical Chemistry Advances. *J. Phys. Chem. C* **2012**, *116*, 11849–11851.
- (6) Hoffmann, M. R.; Martin, S. T.; Choi, W.; Bahnemann, D. W. Environmental Applications of Semiconductor Photocatalysis. *Chem. Rev.* **1995**, *95*, 69–96.

- (7) Yang, J.; Lind, J. U.; Trogler, W. C. Synthesis of Hollow Silica and Titania Nanospheres. *Chem. Mater.* **2008**, *20*, 2875–2877.
- (8) Chen, H.; Liao, Y.; Chen, J.; Wu, K.; Ho, K. Fabrication and Characterization of Plastic-based Flexible Dye-sensitized Solar Cells consisting of Crystalline Mesoporous Titania Nanoparticles as Photoanodes. *J. Mater. Chem.* **2011**, *21*, 17511–17518.
- (9) Chiu, W.; Lee, K.; Hsieh, W. High Efficiency Flexible Dye-Sensitized Solar Cells by Multiple Electrophoretic Depositions. *J. Power Sources* **2011**, *196*, 3683–3687.
- (10) Liao, Y.; Huang, C.; Liao, C.; Wu, J. C. S.; Wu, K. C. W. Synthesis of Mesoporous Titania Thin Films (MTTFs) with Two Different Structures as Photocatalysts for Generating Hydrogen from Water Splitting. *Appl. Energy* **2012**, *100*, 75–80.
- (11) Choi, J.; Park, H.; Hoffman, M. R. Effects of Single Metal-Ion Doping on the Visible-Light Photoreactivity of TiO₂. *J. Phys. Chem. C* **2010**, *114*, 783–792.
- (12) Zhao, J.; Sallard, S.; Smarsly, B. M.; Gross, S.; Bertino, M.; Boissiere, C.; Chena, H. Photocatalytic Performances of Mesoporous TiO₂ Films Doped with Gold Clusters. *J. Mater. Chem.* **2010**, *20*, 2831–2839.
- (13) Colón, G.; Maicu, M.; Hidalgo, M. C.; Navío, J. A. Cu-Doped TiO₂ Systems with Improved Photocatalytic Activity. *Appl. Catal., B* **2006**, *67*, 41–51.
- (14) Dong, F.; Wang, H. Q.; Wu, Z. B. Enhancement of the Visible Light Photocatalytic Activity of C-Doped TiO₂ Nanomaterials Prepared by a Green Synthetic Approach. *J. Phys. Chem. C* **2011**, *115*, 13285–13292.
- (15) Zhang, J.; Wu, Y.; Xing, M.; Leghari, S. A. K.; Sajjad, S. Development of Modified N Doped TiO₂ Photocatalyst with Metals, Nonmetals and Metal Oxides. *Energy Environ. Sci.* **2010**, *3*, 715–726.
- (16) Asapu, R.; Palla, V. M.; Wang, B.; Guo, Z.; Sadu, R.; Chen, D. H. Phosphorus-doped Titania Nanotubes with Enhanced Photocatalytic Activity. *J. Photochem. Photobiol., A* **2011**, *225*, 81–87.
- (17) Jin, Z.; Zhang, X.; Li, Y.; Li, S.; Lu, G. 5.1% Apparent Quantum Efficiency for Hydrogen Generation over Eosine-sensitized CuO/TiO₂ Photocatalyst under Visible Light Irradiation. *Catal. Commun.* **2007**, *8*, 1267–1273.
- (18) Choi, H.; Kang, M. Hydrogen Production from Methanol/Water Decomposition in a Liquid Photosystem using the Anatase Structure of Cu Loaded TiO₂. *Int. J. Hydrogen Energy* **2007**, *32*, 3841–3848.
- (19) Wang, M.; Sun, L.; Lin, Z.; Cai, J.; Xie, K.; Lin, C. p-n Heterojunction Photoelectrodes Composed of Cu₂O-loaded TiO₂ Nanotube Arrays with Enhanced Photoelectrochemical and Photoelectrocatalytic Activities. *Energy Environ. Sci.* **2013**, *6*, 1211–1220.
- (20) Wang, E.; Yang, W.; Cao, Y. Unique Surface Chemical Species on Indium Doped TiO₂ and Their Effect on the Visible Light Photocatalytic Activity. *J. Phys. Chem. C* **2009**, *113*, 20912–20917.
- (21) Atanacio, A. J.; Bak, T.; Nowotny, J. Effect of Indium Segregation on the Surface versus Bulk Chemistry for Indium-doped TiO₂. *ACS Appl. Mater. Interfaces* **2012**, *4*, 6626–6634.
- (22) Mu, J.; Chen, B.; Zhang, M.; Guo, Z.; Zhang, P.; Zhang, Z.; Sun, Y.; Shao, C.; Liu, Y. Enhancement of the Visible-Light Photocatalytic Activity of In₂O₃-TiO₂ Nanofiber Heteroarchitectures. *ACS Appl. Mater. Interfaces* **2012**, *4*, 424–430.
- (23) Liu, G.; Yu, J. C.; Lu, G. Q.; Cheng, H. M. Crystal Facet Engineering of Semiconductor Photocatalysts: Motivations, Advances and Unique Properties. *Chem. Commun.* **2011**, *47*, 6763–6783.
- (24) Jiang, J.; Zhao, K.; Xiao, X.; Zhang, L. Synthesis and Facet-Dependent Photoreactivity of BiOCl Single-Crystalline Nanosheets. *J. Am. Chem. Soc.* **2012**, *134*, 4473–4476.
- (25) Liu, G.; Yang, H. G.; Pan, J.; Yang, Y. Q.; Lu, G. Q.; Cheng, H. Titanium Dioxide Crystals with Tailored Facets. *Chem. Rev.* **2014**, *114*, 9559–9612.
- (26) Li, R.; Han, H.; Zhang, F.; Wang, D.; Li, C. Highly Efficient Photocatalysts Constructed by Rational Assembly of Dual-Cocatalysts Separately on Different Facets of BiVO₄. *Energy Environ. Sci.* **2014**, *7*, 1369–1376.
- (27) Yu, J.; Qi, L.; Jaroniec, M. Hydrogen Production by Photocatalytic Water Splitting Over Pt/TiO₂ Nanosheets with Exposed (001) Facets. *J. Phys. Chem. C* **2010**, *114*, 13118–13125.
- (28) Wu, X.; Chen, Z.; Lu, G. Q.; Wang, L. Nanosized Anatase TiO₂ Single Crystals with Tunable Exposed (001) Facets for Enhanced Energy Conversion Efficiency of Dye-Sensitized Solar Cells. *Adv. Funct. Mater.* **2011**, *21*, 4167–4172.
- (29) Liu, G.; Sun, C.; Yang, H. G.; Smith, S. C.; Wang, L.; Lu, G. Q.; Cheng, H. Nanosized Anatase TiO₂ Single Crystals for Enhanced Photocatalytic Activity. *Chem. Commun.* **2010**, *46*, 755–757.
- (30) Roy, N.; Sohn, Y.; Pradhan, D. Synergy of Low-Energy {101} and High-Energy {001} TiO₂ Crystal Facets for Enhanced Photocatalysis. *ACS Nano* **2013**, *7*, 2532–2540.
- (31) Liu, M.; Piao, L.; Zhao, L.; Ju, S.; Yan, Z.; He, T.; Zhou, C.; Wang, W. Anatase TiO₂ Single Crystals with Exposed {001} and {110} Facets: Facile Synthesis and Enhanced Photocatalysis. *Chem. Commun.* **2010**, *46*, 1664–1666.
- (32) Walsh, A.; Woodley, S. M. Evolutionary Structure Prediction and Electronic Properties of Indium Oxide Nanoclusters. *Phys. Chem. Chem. Phys.* **2010**, *12*, 8446–8453.
- (33) Dai, Y.; Cobley, C. M.; Zeng, J.; Sun, Y.; Xia, Y. Synthesis of Anatase TiO₂ Nanocrystals with Exposed {001} Facets. *Nano Lett.* **2009**, *9*, 2455–2459.
- (34) Zhu, J.; Wang, S.; Bian, Z.; Xie, S.; Cai, C.; Wang, J.; Yang, H.; Li, H. Solvothermally Controllable Synthesis of Anatase TiO₂ Nanocrystals with Dominant {001} Facets and Enhanced Photocatalytic Activity. *CrystEngComm* **2010**, *12*, 2219–2224.
- (35) Deivaraj, T. C.; Park, J.; Afzaal, M.; Brien, P. O.; Vittal, J. J. Novel Bimetallic Thiocarboxylate Compounds as Single-Source Precursors to Binary and Ternary Metal Sulfide Materials. *Chem. Mater.* **2003**, *15*, 2383–2391.
- (36) Gu, L.; Wang, J.; Cheng, H.; Zhao, Y.; Liu, L.; Han, X. One-Step Preparation of Graphene-Supported Anatase TiO₂ with Exposed {001} Facets and Mechanism of Enhanced Photocatalytic Properties. *ACS Appl. Mater. Interfaces* **2013**, *5*, 3085–3093.
- (37) Stengl, V.; Oplustil, F.; Nemeč, T. In³⁺ Doped TiO₂ and TiO₂/In₂S₃ Nanocomposite for Photocatalytic and Stoichiometric Degradations. *Photochem. Photobiol.* **2012**, *88*, 265–276.
- (38) Sasikala, R.; Shirole, A. R.; Sudarsan, V.; Jagannath, C.; Sudakar, R.; Naik, R.; Rao, R.; Bharadwaj, S. R. Role of Support on the Photocatalytic Activity of Titanium Oxide. *Appl. Catal., A* **2010**, *390*, 245–252.
- (39) Muduli, S.; Lee, W.; Dhas, V.; Mujawar, S.; Dubey, M.; Vijayamohan, K.; Han, S.; Ogale, S. Enhanced Conversion Efficiency in Dye-Sensitized Solar Cells Based on Hydrothermally Synthesized TiO₂-MWCNT Nanocomposites. *ACS Appl. Mater. Interfaces* **2009**, *9*, 2030–2035.
- (40) Poznyak, S. K.; Golubev, A. N.; Kulak, A. I. Correlation between Surface Properties and Photocatalytic and Photoelectrochemical Activity of In₂O₃ Nanocrystalline Films and Powders. *Surf. Sci.* **2000**, *396*, 454–456.
- (41) Gan, J.; Lu, X.; Wu, J.; Xie, S.; Zhai, T.; Yu, M.; Zhang, Z.; Mao, Y.; Wang, S. C. I.; Shen, Y.; Tong, Y. Oxygen Vacancies Promoting Photoelectrochemical Performance of In₂O₃ Nanocubes. *Sci. Rep.* **2013**, *3* (1021), 1–7.
- (42) Arrora, A. K.; Rajalakshmi, M.; Ravindran, T. R. *Photon Confinement in Nanostructured Materials in Encyclopedia of Nanoscience and Nanotechnology*; Nalwa, H. S., Ed.; American Science Publishers: CA, 2004; Vol. 8, pp 499–512.
- (43) Bringer, C. J.; Scherer, G. W. *Sol-Gel Science: The Physics and Chemistry of Sol-Gel Processing*; Academic Press: New York, 1990.
- (44) Schubert, U. Chemical Modification of Titanium Alkoxides for Sol-Gel Processing. *J. Mater. Chem.* **2005**, *15*, 3701–3715.
- (45) Parka, J. Y.; Asokana, K.; Choia, S.; Kim, S. S. Growth Kinetics of Nanograins in SnO₂ Fibers and Size Dependent Sensing Properties. *Sens. Actuators, B* **2011**, *152*, 254–260.
- (46) Zhou, Y.; Fichtorn, K. A. Microscopic View of Nucleation in the Anatase-to-Rutile Transformation. *J. Phys. Chem. C* **2012**, *116*, 8314–8321.

- (47) Zhao, C.; Luo, H.; Chen, F.; Zhang, P.; Yi, L.; You, K. A Novel Composite of TiO₂ Nanotubes with Remarkably High Efficiency for Hydrogen Production in Solar-Driven Water Splitting. *Energy Environ. Sci.* **2014**, *7*, 1700–1707.
- (48) Priebe, J. B.; Karnahl, M.; Junge, H.; Beller, M.; Hollmann, D.; Bruckner, A. Water Reduction with Visible Light: Synergy between Optical Transitions and Electron Transfer in Au–TiO₂ Catalysts Visualized by In situ EPR Spectroscopy. *Angew. Chem., Int. Ed.* **2013**, *52*, 11420–11424.
- (49) Ng, J.; Xu, S.; Zhang, X.; Yang, H. Y.; Sun, D. D. Hybridized Nanowires and Cubes: A Novel Architecture of a Heterojunctioned TiO₂/SrTiO₃ Thin Film for Efficient Water Splitting. *Adv. Funct. Mater.* **2010**, *20*, 4287–4292.
- (50) Kibria, M. G.; Nguyen, H. P. T.; Cui, K.; Zhao, S.; Liu, D.; Guo, H.; Trudeau, M. L.; Paradis, S.; Hakima, A.; Mi, Z. One-Step Overall Water Splitting under Visible Light Using Multiband InGaN/GaN Nanowire Heterostructures. *ACS Nano* **2013**, *7*, 7886–7893.
- (51) Maitra, U.; Gupta, U.; De, M.; Datta, R.; Govindaraj, A.; Rao, C. N. R. Highly Effective Visible-Light-Induced H₂ Generation by Single-Layer 1T–MoS₂ and a Nanocomposite of Few-Layer 2H–MoS₂ with Heavily Nitrogenated Graphene. *Angew. Chem., Int. Ed.* **2013**, *52*, 13057–13061.
- (52) Moon, G. D.; Joo, J. B.; Lee, I.; Yin, Y. Decoration of Size-tunable CuO nanodots on TiO₂ nanocrystals for Noble Metal-free Photocatalytic H₂ Production. *Nanoscale* **2014**, *6*, 12002–12008.
- (53) Narendranath, S. B.; Yadav, A. K.; Bhattacharyya, D.; Jha, S. N.; Devi, R. N. Photocatalytic H₂ Evolution from Water–Methanol System by Anisotropic InFeO₃(ZnO)_m Oxides without Cocatalyst in Visible Light. *ACS Appl. Mater. Interfaces* **2014**, *6*, 12321–12327.
- (54) Ronca, E.; Pastore, M.; Belpassi, L.; Tarantella, F.; Angelis, F. D. Influence of the Dye Molecular Structure on the TiO₂ Conduction Band in Dye-Sensitized Solar Cells: Disentangling Charge Transfer and Electrostatic Effects. *Energy Environ. Sci.* **2013**, *6*, 183–193.
- (55) Linsebigler, A. L.; Lu, G.; Yates, J. T. Photocatalysis on TiO₂ Surfaces: Principles, Mechanisms, and Selected Results. *Chem. Rev.* **1995**, *95*, 735–758.
- (56) Zhang, J.; Bang, J. H.; Tang, C.; Kamat, P. V. Tailored TiO₂–SrTiO₃ Heterostructure Nanotube Arrays for Improved Photoelectrochemical Performance. *ACS Nano* **2010**, *4*, 387–395.
- (57) Kubacka, A.; Fernandez-Garcia, M.; Colon, G. Advanced Nanoarchitectures for Solar Photocatalytic Applications. *Chem. Rev.* **2012**, *112*, 1555–1614.
- (58) Robel, I.; Kuno, M.; Kamat, P. V. Size-Dependent Electron Injection from Excited CdSe Quantum Dots into TiO₂ Nanoparticles. *J. Am. Chem. Soc.* **2007**, *129*, 4136–4137.
- (59) Selinsky, R. S.; Ding, Q.; Faber, M. S.; Wright, J. C.; Jin, S. Quantum Dot Nanoscale Heterostructures for Solar Energy Conversion. *Chem. Soc. Rev.* **2013**, *42*, 2963–2985.
- (60) Xu, H.; Reunchan, P.; Ouyang, S.; Tong, H.; Umezawa, N.; Kako, T.; Ye, J. Anatase TiO₂ Single Crystals Exposed with High-Reactive {111} Facets Toward Efficient H₂ Evolution. *Chem. Mater.* **2013**, *25*, 405–411.
- (61) Liu, X.; Geng, D.; Wang, X.; Ma, S.; Wang, H.; Li, D.; Li, B.; Liu, W.; Zhang, Z. Enhanced Photocatalytic Activity of Mo–{001}TiO₂ Core-Shell Nanoparticles under Visible Light. *Chem. Commun.* **2010**, *46*, 6956–6958.
- (62) Kato, H.; Asakura, K.; Kudo, A. Highly Efficient Water Splitting into H₂ and O₂ over Lanthanum-Doped NaTaO₃ Photocatalysts with High Crystallinity and Surface Nanostructure. *J. Am. Chem. Soc.* **2003**, *125*, 3082–3089.
- (63) Kudo, A.; Miseki, Y. Heterogeneous Photocatalyst Materials for Water Splitting. *Chem. Soc. Rev.* **2009**, *38*, 253–278.
- (64) Vittadini, A.; Selloni, A.; Rotzinger, F. P.; Gratzel, M. Structure and Energetics of Water Adsorbed at TiO₂ Anatase 101 and 001 Surfaces. *Phys. Rev. Lett.* **1998**, *81*, 2954–2957.
- (65) Selloni, A. Crystal growth: Anatase Shows its Reactive Side. *Nat. Mater.* **2008**, *7*, 613–615.
- (66) Chen, Q.; Ma, W.; Chen, C.; Ji, H.; Zhao, Z. Anatase TiO₂ Mesocrystals Enclosed by (001) and (101) Facets: Synergistic Effects between Ti³⁺ and Facets for Their Photocatalytic Performance. *Chem.—Eur. J.* **2012**, *18*, 12584–12589.
- (67) Arienzo, M. D.; Carbajo, J.; Bahamonde, A.; Crippa, M.; Polizzi, S.; Scotti, R.; Wahba, L.; Morazzoni, F. Photogenerated defects in Shape-Controlled TiO₂ Anatase Nanocrystals: A Probe to Evaluate the Role of Crystal Facets in Photocatalytic Processes. *J. Am. Chem. Soc.* **2011**, *133*, 17652–17661.
- (68) Murakami, N.; Katayama, S.; Nakamura, M.; Tsubota, T.; Ohno, T. Dependence of Photocatalytic Activity on Aspect Ratio of Shape-Controlled Rutile Titanium(IV) Oxide Nanorods. *J. Phys. Chem. C* **2011**, *115*, 419–424.
- (69) Liu, L.; Gu, X.; Ji, Z.; Zou, W.; Tang, C.; Gao, F.; Dong, L. Anion-Assisted Synthesis of TiO₂ Nanocrystals with Tunable Crystal Forms and Crystal Facets and Their Photocatalytic Redox Activities in Organic Reactions. *J. Phys. Chem. C* **2013**, *117*, 18578–18587.